Research Article Vol. 29, No. 4 / 15 February 2021 / Optics Express 5808
Optics EXPRESS

Negative curvature hollow core fiber sensor for the measurement of strain and temperature

MARTA S. FERREIRA,[1,2,*] JÖRG BIERLICH,[2] JENS KOBELKE,[2] JOÃO L. PINTO,[1] AND KATRIN WONDRACZEK[2]

[1] *i3N & Physics Department, University of Aveiro, Campus de Santiago, 3810-193 Aveiro, Portugal*
[2] *Leibniz Institute of Photonic Technology, Albert-Einstein-Straße 9, 07745 Jena, Germany*
[*] *marta.ferreira@ua.pt*

Abstract: Three different types of strain and temperature sensors based on negative curvature hollow core fiber (NCHCF) are proposed. Each sensor is produced by splicing a small section of the NCHCF between two sections of single mode fiber. Different types of interferometers are obtained simply by changing the splicing conditions. The first sensor consists on a single Fabry-Perot interferometer (FPI). The remaining two configurations are attained with the same sensing structure, depending on its position in relation to the interrogation setup. Thus, a double FPI or a hybrid sensor, the latter being composed by an FPI and a Michelson interferometer, are formed. The inline sensors are of submillimeter size, thus enabling nearly punctual measurements.

1. Introduction

The simultaneous measurement of strain and temperature with optical fiber sensors has been thoroughly investigated, not only to provide solutions for applications where the two measurands need to be discriminated but also for compensating the effects of temperature when strain is the only measurand to be determined. Several configurations based on fiber Bragg grating technology have been explored in this context, usually by combining different sensing elements [1–4]. On the other hand, interferometric configurations such as the Mach-Zehnder interferometer [5], the combination of two Fabry-Perot cavities [6], and intermodal interferometers [7] have also been explored for this specific application.

The use of cascaded Fabry-Perot interferometers (FPIs) has also been proposed for simultaneous measurement of different parameters, such as strain and temperature [8] or high pressure and temperature [9]. In the former, the cavities were obtained by using short sections of capillary silica tube and single mode fiber [8], whereas in the last, the sensor was composed by a short section of hollow-core photonic bandgap fiber and a capillary silica tube [9].

A hybrid sensing structure that results from the combination of two different interferometers can also be employed in the discrimination of different measurands. For example, a hybrid sensor constituted by a FPI and a Michelson interferometer (MI), was proposed, by splicing a short section of photonic crystal fiber to the output port of a 3 dB optical coupler [10]. The sensing device was used to discriminate liquid refractive index and temperature. On the other hand, a hybrid sensor based on a two cores fiber and a silica capillary spliced in series was reported for the simultaneous detection of strain and radial bending [11]. The discrimination of strain and temperature measurements was also addressed using a hybrid interferometer, achieved by splicing a section of dual asymmetric core microstructured fiber to single mode fiber [12].

In this work, a negative curvature hollow core fiber is proposed in three different configurations, for the measurement of strain and/or temperature. Depending both on the splicing conditions and on the connections made in the experimental setup, a single FPI, a double FPI or a hybrid interferometer can be attained. The sensors, of sub-millimeter size, require only the use of a fusion splicer to be fabricated. This versatile sensing structure can be used in applications where

#412532 https://doi.org/10.1364/OE.412532
Journal © 2021 Received 15 Oct 2020; revised 23 Dec 2020; accepted 1 Jan 2021; published 9 Feb 2021

Optics EXPRESS

nearly punctual strain detection is required, with the advantage of being able to perform either temperature independent measurements or simultaneous measurement of strain and temperature.

2. Sensors Design

The negative curvature hollow core fiber (NCHCF) used in this work, whose cross-section image is shown in Fig. 1, was fabricated at the Leibniz Institute of Photonic Technology, in Jena, Germany. It consists of four silica capillaries placed in diametrically opposed positions, with a thickness of ~1 µm, surrounded by a cladding with a wall thickness of ~26 µm. The hollow core has a width of ~15 µm. The 4 wall segments of the hollow core have a uniform negative radius of curvature of about 24 µm. The fiber external diameter is ~125 µm. The fiber was coated with a single UV acrylate layer during the fabrication, following the procedures described elsewhere [13,14].

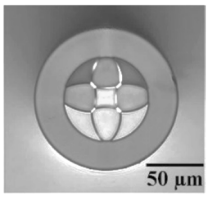

Fig. 1. Microscopic picture of the negative curvature hollow core fiber cross-section.

The sensors were produced by splicing a short section of the NCHCF between two sections of single mode fiber (SMF28), using the manual mode of the fusion splicer (Fitel S177). Two different sensing geometries were explored in the framework of this work, one with standard splices and the other with a splicing feature. For the standard splice, the arc discharge power was set to 15 arb. units, with a discharge time of 500 ms (for comparison purposes, an automatic splice with this splicer has a discharge power and time of 100 arb. units and 2000 ms, respectively). The two fibers were aligned with a lateral offset, and brought together as close as possible, without any tension between them. The arc discharge was mainly applied in the SMF section, to ensure that the NCHCF internal structure did not change during the procedure. Figure 2(a) shows the microscope image of a sensor fabricated in such way. To produce the splicing feature, the two fibers were aligned with a lateral offset and by maintaining a gap between them (~20 µm). The arc power was increased to 25 arb. units, whilst the discharge time was not changed. In this case, as the arc discharge is applied, the internal structure of the NCHCF changes locally, creating a degenerated area, as shown in Fig. 2(b) and 2(c). This effect has already been reported in the literature, where it was used for improving the circulation of liquids inside the fiber [15,16]. However, to the best of our knowledge, it has not been explored as a sensing element itself.

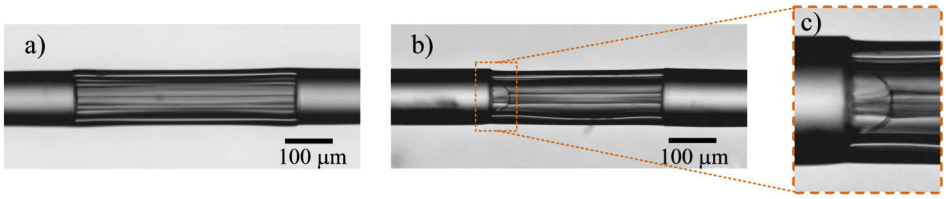

Fig. 2. Microscope images of the (a) FPI, (b) sensor with splicing feature, and (c) zoom-in of splicing feature.

The change in the fiber structure, produced by the splicing procedure, is easily observable in the longitudinal view (Fig. 2(b), on the left side, and Fig. 2(c)). Due to the very low thickness

Optics EXPRESS

of the inner silica capillaries, during the arc discharge there is a stronger melting in that region, causing the semi-circular shape of the splicing feature. With the current fabrication method, it is not possible to fully control the length of this feature. During these experiments, lengths ranging from ~15 µm up to ~70 µm were attained. This variation has influence on the sensor behavior. For sensors with degenerated area lengths smaller than 16 µm, the effect here described is not observable. Efforts are being made to improve the fabrication method.

3. Working Principle

The sensor shown in Fig. 2(a) is a low-finesse FPI, which can be approximated to a two-wave interferometer. Consider that the first interface SMF/NCHCF constitutes the mirror M_1, with a reflection coefficient $R_1 = (n_{SMF} - n_1)^2/(n_{SMF} + n_1)^2$, and with transmission losses due surface imperfections of A_1 [17]. Light travels in the hollow core of the NCHCF ($n_1 = 1$) until it reaches the mirror M_2 (NCHCF/SMF interface), with a reflection coefficient, R_2, which is equal to R_1. The total cavity losses, including the effects due to mode mismatch and beam expansion, were accounted for as the coefficient α_1.

The total reflected-light intensity was estimated through the equations of the electric field for a low-finesse FPI. These equations, approximately given by the sum of the electric fields reflected at each interface were derived according to Fig. 3, being the intensity given by:

$$I_R(\lambda) = R_1 + (1 - A_1)^2(1 - \alpha_1)^2(1 - R_1)^2 R_2 - 2\sqrt{R_1 R_2}(1 - A_1)(1 - R_1)(1 - \alpha_1)\cos(\varphi_1), \quad (1)$$

where $\varphi_1 = 4\pi n_1 L_{FP}/\lambda$ is the round-trip propagation shift, being L_{FP} the cavity length and λ the vacuum wavelength.

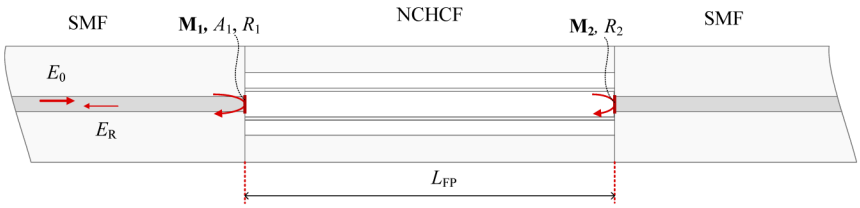

Fig. 3. Schematic design of the FPI sensor, with indication of the reflection surfaces.

A similar line of thought can be followed to better understand the working principle of the sensor with degenerated area shown in Fig. 2(b). As the structure is not symmetric, depending on the side over which light is injected and collected, different interferometric paths will be created, giving rise to two different sensors: a double FPI and a hybrid interferometer, composed by an FPI and a MI. Furthermore, the splicing feature will introduce higher cavity losses, which have influence in the spectrum visibility.

For the case of the double FPI configuration (Fig. 4), light coming from the SMF core suffers a first reflection at the mirror M_1. A fraction of light is guided through the hollow core until it reaches M_3. This large FP cavity gives rise to a high frequency signal. On the other hand, due to the beam expansion as it exits the SMF core, a small fraction of light will reach M_2, where it will be reflected and coupled back to the SMF. In fact, this small feature can also be seen as a Fabry-Perot interferometer, with a cavity length L_1. There is also a fraction of light that is coupled to the NCHCF strands, which is transmitted to the SMF at the end of L_3. However, since the refractive indices of both NCHCF strands and SMF are approximate, the reflection coefficient at that interface is very low. Therefore, even if some of the light is reflected at that interface, it will not have a significant impact on the reflection spectrum.

Notice that this double FPI is not a traditional cascaded configuration, where the signal propagates in the first cavity prior to achieving the second one. Here, the two cavities have the

Optics EXPRESS

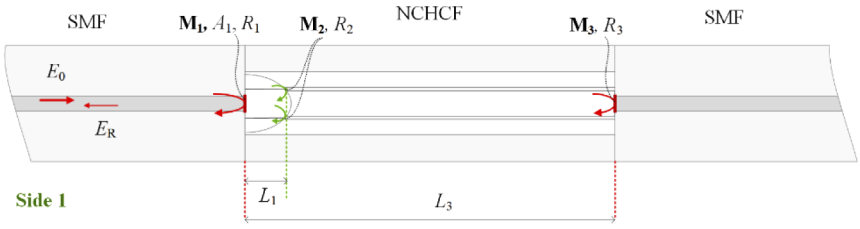

Fig. 4. Scheme of the NCHCF double FPI sensor, with indication of the reflective surfaces.

first interface in common, however, light propagates to the remaining interfaces through different interferometric paths. The total reflected light intensity can be estimated through Eq. (2):

$$\begin{aligned} I_R(\lambda) = {} & R_1 + (1-A_1)^2(1-R_1)^2(1-\alpha_2)^2R_3 + (1-A_1)^2(1-\alpha_1)^2(1-R_1)^2R_2 \\ & - 2\sqrt{R_1R_2}(1-A_1)(1-R_1)(1-\alpha_1)\cos(\varphi_1) \\ & - 2\sqrt{R_1R_3}(1-A_1)(1-\alpha_2)(1-R_1)\cos(\varphi_2) \\ & + 2\sqrt{R_2R_3}(1-A_1)^2(1-R_1)^2(1-\alpha_1)(1-\alpha_2)\cos(\varphi_2-\varphi_1), \end{aligned} \tag{2}$$

where $\varphi_1 = 4\pi n_1 L_1/\lambda$ and $\varphi_2 = 4\pi n_2 L_3/\lambda$. The reflection coefficients, R_1, R_2 and R_3 are approximately the same, as the interfaces are all composed by silica/air. The coefficient A_1 is the transmission loss factor at M_1, α_1 and α_2, are the cavity loss factors for the smaller and longer FPI, respectively. The parameters n_1 and n_2, and L_1 and L_3 are the refractive indices and physical lengths of each FPI, respectively. In these simulations, it was considered that the smaller FPI presents higher cavity losses, as it is only formed by the small fraction of light that achieves the silica strands (of ~1 μm in thickness) that surround the fiber core. Considering the parameters used in the simulation (see Table 1), the first terms in Eq. (2) are dominant over the last term, which was ignored in the calculations. Thus, Eq. (2) can be simplified to:

$$\begin{aligned} I_R(\lambda) = {} & R_1 + (1-A_1)^2(1-R_1)^2R_1((1-\alpha_1)^2 + (1-\alpha_2)^2) \\ & - (2R_1(1-A_1)(1-R_1)(1-\alpha_1)\cos(\varphi_1) + 2R_1(1-A_1)(1-R_1)(1-\alpha_2)\cos(\varphi_2)). \end{aligned} \tag{3}$$

This result indicates that the reflection spectrum depends mainly on the two FPIs separately, being composed by two frequencies: a higher frequency signal (larger FPI) and lower frequency signal (smaller FPI).

Table 1. Summary of the parameters used for the simulations.

	Double FPIs	Hybrid sensor
L_1 (μm)	40.9	
L_2 (μm)		314.93
L_3 (μm)	385.03	385.03
n_1, n_1'	0.99	0.9895
n_2	0.99	1.397
A_1	0.6	0.6
α_1	0.95	
α_2	0.85	0.6
α_2'		0.9
R_1, R_2, R_3	0.0335	0.0335

Optics EXPRESS

The total reflected light intensity was also estimated for the hybrid configuration (see Fig. 5). On one hand, as light reaches M_1, Fresnel reflection occurs, and a fraction of light is transmitted through the NCHCF. Light is then reflected at the last interface (air/silica), propagates once again through the NCHCF and is recoupled back to the SMF. This constitutes the first FP interferometer. On the other hand, there is also a second FP interferometer, that can be understood as follows: part of the light that is transmitted to the NCHCF is also coupled to the silica strands, being reflected at the silica/air interface of the degenerated area, and afterwards coupled back to the input SMF.

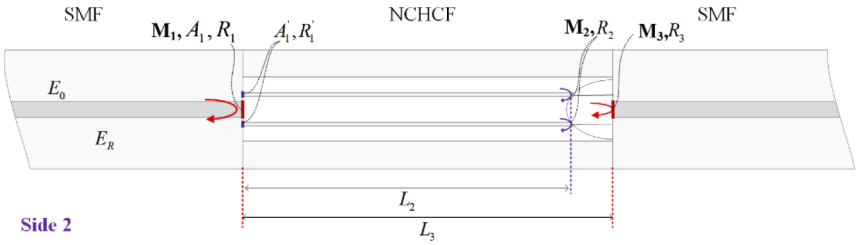

Fig. 5. Scheme of the NCHCF hybrid sensor, with indication of the reflective surfaces.

The intensity of the interference fringes can be described with the following equation:

$$\begin{aligned} I_R(\lambda) = {} & R_1 + (1-A_1)^2(1-R_1)^2(1-\alpha_2)^2R_3 + (1-A_1')^2(1-\alpha_2')^2R_2 \\ & - 2\sqrt{R_1R_3}(1-A_1)(1-R_1)(1-\alpha_2')\cos(\varphi_1) \\ & + 2\sqrt{R_1R_2}(1-A_1')(1-\alpha_2')\cos(\varphi_1') \\ & - 2\sqrt{R_2R_3}(1-A_1)(1-A_1')(1-R_1)(1-\alpha_2)(1-\alpha_2')\cos(\varphi_1-\varphi_1'), \end{aligned} \tag{4}$$

where $\varphi_1 = 4\pi n_1 L_3/\lambda$ and $\varphi_1' = 4\pi n_2 L_2/\lambda$. In this approach, A_1 is the transmission loss factor, α_2 and α_2' are the air and silica cavities loss factors, respectively. This last component of Eq. (4) corresponds to the low frequency component (MI), originated by the subtraction between the two FPIs.

Notice that the previous arguments are only valid when NCHCF length is small enough to provide low-finesse Fabry-Perot interferometers, and the conditions for antiresonant guidance are not achieved [18]. Figure 6 presents the simulated reflection spectra for each configuration.

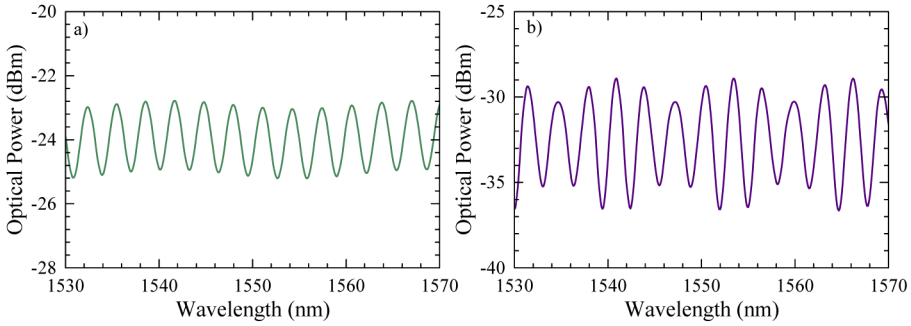

Fig. 6. Simulated spectra of the a) double FPI configuration and b) hybrid sensor.

Optics EXPRESS

4. Results and Discussion

The sensors responses were monitored in a typical reflection setup, as shown in Fig. 7. The broadband optical source, centered at 1550 nm, had a bandwidth of 40 nm. The optical spectrum analyzer (OSA ANDO AQ6317C) had a resolution of 0.02 nm. Each sensor was connected to the interrogation system on both sides. In the case of the interferometer with the splicing feature, evidenced in the scheme of Fig. 7, the splicing between the sensor and the interrogation system was performed closer to the degenerated area (side 1) and afterwards, the sensor was turned around and the splice was done in the SMF opposite to that area (side 2). Both the spectral characteristics and sensor response were investigated on each side.

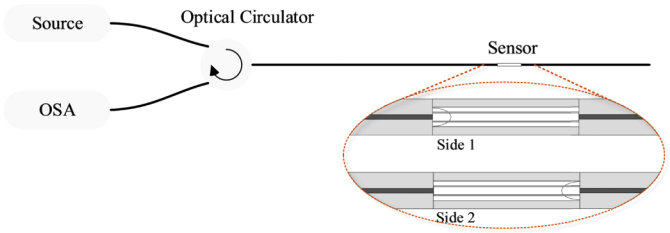

Fig. 7. Scheme of the experimental setup.

The FPI reflection spectra (Fig. 8(a, b)) shows the typical behavior of a two-wave interferometer, as expected. This is corroborated by the single frequency located at 0.42 nm^{-1}, observed in the fast Fourier transform (FFT) (Fig. 8(c, d)). The effective refractive index, n_{eff}, was determined using the equation $n_{eff} = \xi\lambda^2/(2L)$, where ξ is the frequency and λ the center wavelength. For a cavity length (L) of 507 µm, measured through the microscope picture of Fig. 2(a), n_{eff} = 1.006, meaning that the mode is propagating in air. The sensor spectral response, in this case, does not change significantly in respect to the side connected to the optical circulator. The visibility variation, from 96.3% to 78.6%, is attributed mainly to the quality of the splices, and does not have influence on the sensor behavior.

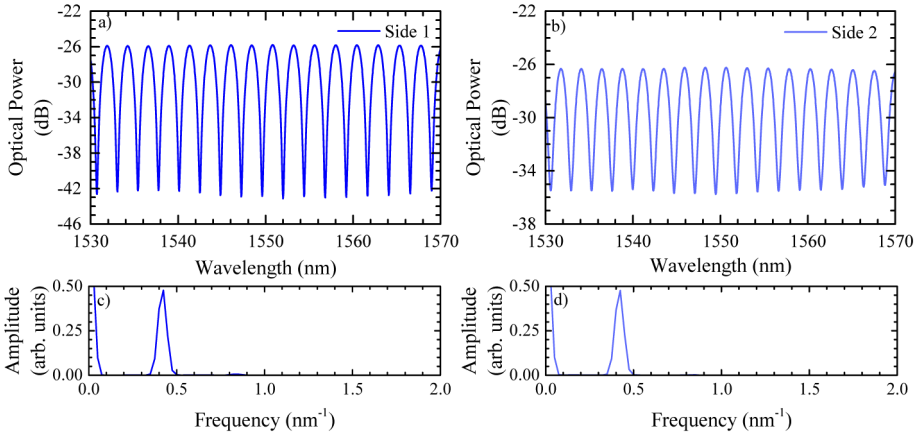

Fig. 8. (a,b) Fabry-Perot interferometer spectra obtained by connecting each side to the optical circulator and (c,d) the corresponding FFT.

The spectral response of the sensor with a splicing feature, depicted in Fig. 9, is highly dependent on the side connected to the circulator. On one hand, when the sensor is connected from the side with the degenerated area, two distinct frequencies appear in the spectrum, which

Optics EXPRESS

are highlighted in the FFT. The high frequency signal, located at ~0.3 nm^{-1}, is originated by the cavity formed between the two splices. If one takes into consideration the cavity length measured through the microscopic image in Fig. 2(b), $L = 385$ μm, an effective refractive index of ~0.99 RIU is attained, meaning that light is propagating within the hollow core. This high frequency is modulated by a lower one, located at ~0.05 nm^{-1}. Considering the degenerated area length, of 45 μm, the effective refractive index is determined to be 1.04. This corroborates with the assumption that light is travelling in air, in that specific region. The spectral behavior is similar to the one attained through the numerical simulations.

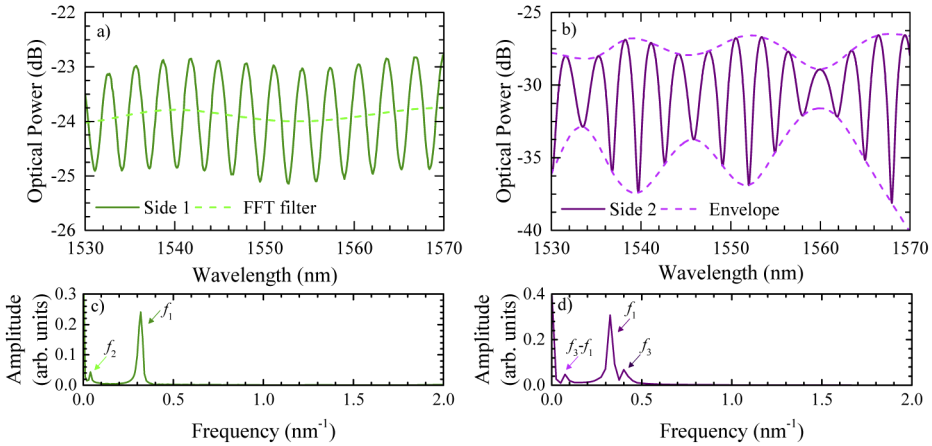

Fig. 9. Spectra obtained by connecting the side with the degenerated area (a) directly to the interrogation setup (side 1) and (b) opposite to the interrogation setup (side 2). (c) and (d) are the respective FFTs.

When one connects the sensor to the optical circulator with the degenerated area turned to the opposite side, the response changes considerably. Considering the cavity length measured from Fig. 2(b), $L = 385$ μm, and the FFT frequency of ~0.31 nm^{-1}, the effective refractive index is ~1.01 RIU, meaning that light is propagating in air, like in the case of the previous configuration. On the other hand, the FFT also indicates the presence of a second frequency $\xi_2 = 0.39$ nm^{-1}. Considering the cavity length $L_3 = 385$ μm, the effective refractive index is, in this case of $n_{eff} = 1.22$ RIU. The difference between the two frequencies gives rise to a third frequency, $\xi_3 = 0.07$ nm^{-1}, which is highlighted by the envelope presented in Fig. 9(b). This frequency corresponds to the Michelson interferometer.

The sensors were subjected to strain and temperature measurements, using the same interrogation setup as described before. For the strain measurements, the sensor was glued to a translation stage (resolution of 10 μm) and to a fixed platform. The temperature measurements were done by placing the sensor in a tubular oven (resolution of 1 °C), and by increasing the temperature from room temperature (~20 °C) in steps of 25 °C, until 175 °C. For each step, the sensor spectra were acquired by connecting each side to the interrogation setup.

Figures 10(a) and (b) show the spectral shift for three different values of strain and temperature, respectively, for the FPI sensor shown in Fig. 2(a). The wavelength shift dependence with strain and temperature, is respectively shown in Fig. 10(c) and (d). The response is, in both cases, independent on the side connected to the interrogation setup. The sensitivities attained were of 2.3 pm/με and 1.3 pm/°C, for strain and temperature, respectively. The response is similar to other air-based FPIs already reported in the literature [6,19,20].

Regarding the strain response of the double FPIs configuration, presented in Fig. 11(a) and (c), there is a wavelength shift towards longer wavelengths (red shift) for both interferometers.

Optics EXPRESS

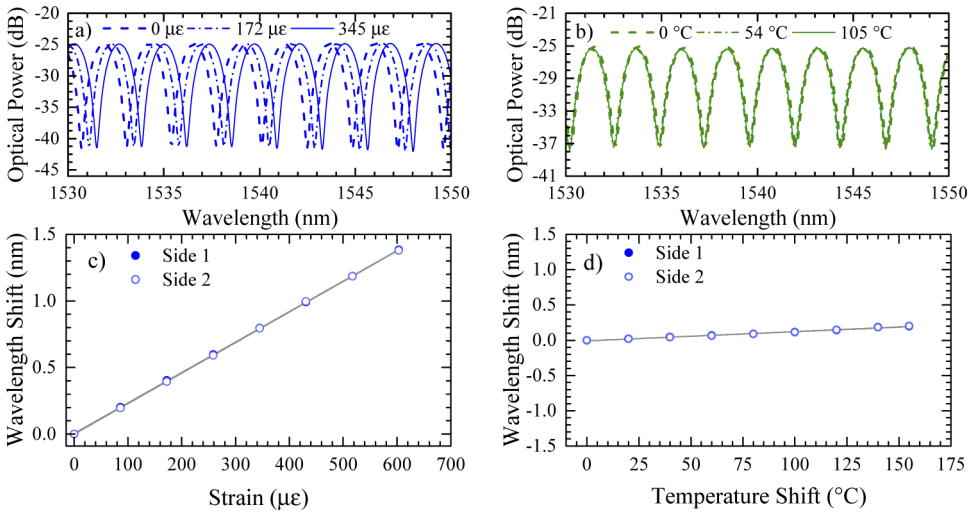

Fig. 10. FPI spectral shift for three different values of (a) strain and (b) temperature. The peak wavelength shift dependence with strain and temperature are represented respectively in (c) and (d).

The smaller the cavity length, the higher the sensitivity to strain, in accordance with other works [19,20].

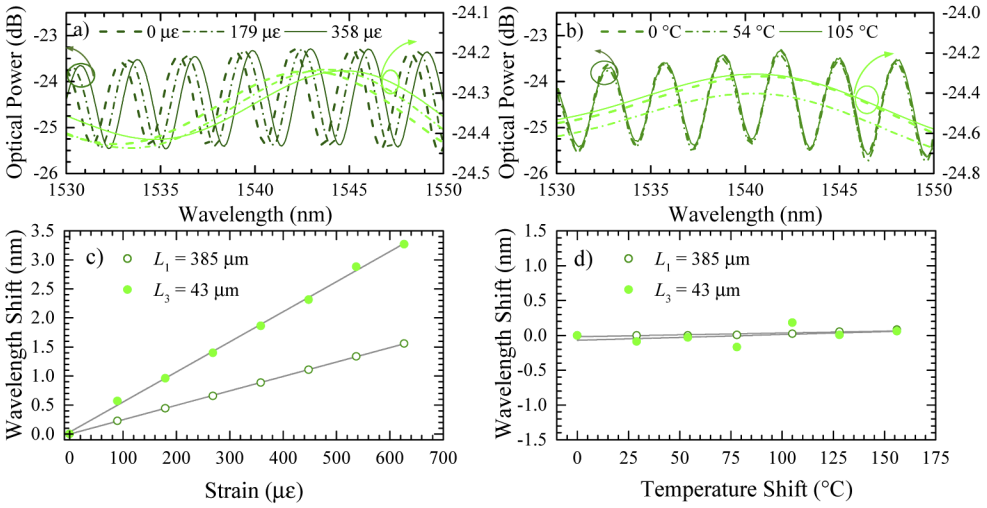

Fig. 11. Double FPI sensor spectral shift for three different values of (a) strain and (b) temperature. The FFT filter is shown in light green, with a different scale for better perception. The peak wavelength shift dependence with strain and temperature are represented respectively in (c) and (d).

The sensitivities attained were of 6.4 pm/με and 2.5 pm/με for the shorter and longer cavities, respectively. The response to temperature is shown in Fig. 11(b) and (d). In both cases the sensitivity to temperature is very low, of 0.5 pm/°C and 0.8 pm/°C for the smaller and larger FPI, respectively. Therefore, this sensor can be used for temperature independent strain measurements,

Optics EXPRESS

with the advantage that one of the cavities can be used as a reference, to minimize the effects of fluctuations from the environment.

In relation to the hybrid interferometer, the response, shown in Fig. 12, is quite different from the ones previously discussed. In fact, the FPI and the MI exhibit opposite responses to strain (Fig. 12(a) and (c)). The FPI presents a shift towards longer wavelengths, with a sensitivity of 2.5 pm/με. It should be highlighted that the sensitivity is similar to the one obtained in the double FPIs configuration. The Michelson interferometer shifts towards smaller wavelengths (blue shift), with a sensitivity of −0.5 pm/με. The smaller sensitivity observed is due to the fact that this interferometer arises mainly from the difference between the optical path lengths of each interferometer. As the silica FPI is slightly smaller than the air FPI and given the complexity of the structure in the degenerated region, this interferometer will suffer a different elongation than the air FPI, resulting in the blue shift observed.

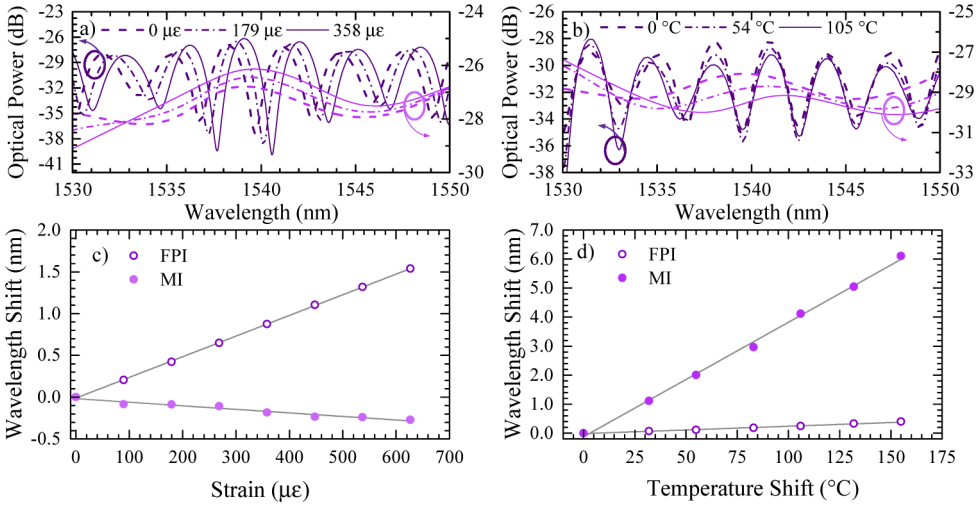

Fig. 12. Hybrid sensor spectral shift for three different values of (a) strain and (b) temperature. The upper envelope is shown in light purple, with a different scale for better perception. The peak wavelength shift dependence with strain and temperature are represented respectively in (c) and (d).

The response of both interferometers to temperature is shown in Fig. 12(b) and (d). The high frequency signal sensitivity is of 1.8 pm/°C. For the lower frequency signal, corresponding to the MI, a sensitivity of 41.7 pm/°C was achieved. Here, the dominant effect is the thermo-optic coefficient of the fiber. As the two interferometers are formed in different media (air and silica), the difference between the effective refractive indices gives rise to the higher sensitivity observed for the MI.

The different responses of each sensing element to the two parameters make this sensing structure a good candidate to perform simultaneous measurement of strain and temperature. Furthermore, it should be highlighted that the sensor relies only in a single microstructured optical fiber and in splicing procedures. The low dimensions of this sensor are also an advantage in situations where nearly punctual strain and/or temperature detection is required.

Several sensors were fabricated, comprising different lengths and splicing feature dimensions. The behavior here described was observed for most of the sensors. However, for cavity lengths higher than 600 μm, the complexity of the interference pattern increased, due to the arising of antiresonant guidance effects, which become dominant for longer lengths [18].

Optics EXPRESS

5. Conclusions

In summary, a microcavity based on a negative curvature hollow core fiber was evaluated for strain and/or temperature sensing. Depending on the fabrication conditions, a single FPI was attained, with sensitivities similar to other air-based FPIs reported in the literature. For a cavity with ~507 μm, the sensitivity towards strain and temperature were of 2.3 pm/με and 1.3 pm/°C, respectively. Structures with a degenerated area were also tested towards these parameters. In this case, the sensors responses were related to the side connected to the interrogation setup. On one hand, when the sensor was connected from the side with the splicing feature, a double FPI was attained, with different sensitivities to strain 6.4 pm/με and 2.5 pm/με, for the smaller and longer FPI, respectively. The sensor presented low sensitivity to temperature (< 1 pm/°C), thus being suitable for high sensitivity strain measurements, with low cross-sensitivity to temperature. On the other hand, if the sensor was connected to the interrogation setup by the side opposite to the degenerated area, a hybrid interferometer, composed by an FPI and a MI was attained. In this case, strain sensitivities of 2.5 pm/με and −0.5 pm/με were obtained for the FPI and for the MI, respectively. Regarding temperature, a sensitivity of 1.8 pm/°C was attained for the former, whereas for the last the sensitivity was of 41.7 pm/°C. The proposed sensing devices are easy to manufacture, requiring only one type of microstructured optical fiber and a fusion splicer. To the best of our knowledge, this is the first time that a NCHF is proposed for strain and temperature measurements. Furthermore, the use of the splicing feature formed in one of the splices to generate different interferometric paths and as a sensing element is also a novelty. This can bring alternative paths for research and development of new optical fiber sensors. The sensors dimensions can also present an advantage for applications where nearly punctual detection of strain and temperature are aimed.

Funding. Fundação para a Ciência e a Tecnologia (PTDC/EEI-EEE/31568/2017, UIDB/50025/2020, UIDP/50025/2020); CENTRO2020 Programa Operacional Regional do Centro (CENTRO-01-0145-FEDER-031568).

Disclosures. The authors declare no conflicts of interest.

References

1. L. Xiaohong, W. Dexiang, Z. Fujun, and D. Enguang, "Simultaneous independent temperature and strain measurement using one fiber Bragg grating based on the etching technique," Microw. Opt. Technol. Lett. **43**(6), 478–481 (2004).
2. M. G. Xu, J.-L. Archambault, L. Reekie, and J. P. Dakin, "Discrimination between strain and temperature effects using dual-wavelength fibre grating sensors," Electron. Lett. **30**(13), 1085–1087 (1994).
3. H. F. Lima, P. F. Antunes, J. L. Pinto, and R. N. Nogueira, "Simultaneous measurement of strain and temperature with a single fiber Bragg grating written in a tapered optical fiber," IEEE Sens. J. **10**(2), 269–273 (2010).
4. W.-C. Du, X.-M. Tao, and H.-Y. Tam, "Fiber Bragg grating cavity sensor for simultaneous measurement of strain and temperature," IEEE Photonics Technol. Lett. **11**(1), 105–107 (1999).
5. J. Zhou, C. Liao, Y. Wang, G. Yin, X. Zhong, K. Yang, B. Sun, G. Wang, and Z. Li, "Simultaneous measurement of strain and temperature by employing fiber Mach-Zehnder interferometer," Opt. Express **22**(2), 1680–1686 (2014).
6. A. Zhou, B. Qin, Z. Zhu, Y. Zhang, Z. Liu, J. Yang, and L. Yuan, "Hybrid structured fiber-optic Fabry-Perot interferometer for simultaneous measurement of strain and temperature," Opt. Lett. **39**(18), 5267–5270 (2014).
7. C. Lu, J. Su, X. Dong, T. Sun, and K. T. V. Grattan, "Simultaneous measurement of strain and temperature with a few-mode fibre-based sensor," J. Lightwave Technol. **36**(13), 2796–2802 (2018).
8. J. Tian, Y. Jiao, S. Ji, X. Dong, and Y. Yao, "Cascaded-cavity Fabry-Perot interferometer for simultaneous measurement of temperature and strain with cross-sensitivity compensation," Opt. Commun. **412**, 121–126 (2018).
9. Z. Zhang, J. He, B. Du, F. Zhang, K. Guo, and Y. Wang, "Measurement of high-pressure and high temperature using a dual-cavity Fabry-Perot interferometer created in cascade hollow-core fibers," Opt. Lett. **43**(24), 6009–6012 (2018).
10. H. Sun, J. Zhang, Q. Rong, D. Feng, Y. Du, X. Zhang, D. Su, L. Zhou, Z. Feng, X. Qiao, and M. Hu, "A hybrid interferometer for simultaneous refractive index and temperature measurements based on Fabry-Perot/ Michelson interference," IEEE Sens. J. **13**(5), 2039–2044 (2013).
11. Y. Zhang, Y. Zhang, Z. Wang, Z. Liu, Y. Wei, E. Zhao, X. Yang, J. Zhang, and L. Yuan, "A novel Michelson Fabry-Perot hybrid interference sensor based on the micro-structured fiber," Opt. Commun. **374**, 58–63 (2016).
12. O. Frazão, S. F. Silva, J. Viegas, J. M. Baptista, J. L. Santos, and P. Roy, "A hybrid Fabry-Perot/Michelson interferometer sensor using a dual asymmetric core microstructured fiber," Meas. Sci. Technol. **21**(2), 025205 (2010).
13. A. Hartung, J. Kobelke, A. Schwuchow, K. Wondraczek, J. Bierlich, J. Popp, T. Frosch, and M. A. Schmidt, "Double antiresonant hollow core fiber-guidance in the deep ultraviolet by modified tunneling leaky modes," Opt. Express **22**(16), 19131–19140 (2014).

Optics EXPRESS

14. K. Schuster, S. Unger, C. Aichele, F. Lindner, S. Grimm, D. Litzkendorf, J. Kobelke, J. Bierlich, K. Wondraczek, and H. Bartelt, "Material and technology trends in fiber optics," Adv. Opt. Technol. **3**(4), 447–468 (2014).
15. J. P. Moura, H. Baierl, J.-L. Auguste, R. Jamier, P. Roy, J. L. Santos, and O. Frazão, "Evaporation of volatile compounds in suspended-core fibers," Opt. Lett. **39**(13), 3868–3871 (2014).
16. M. Hou, Y. Wang, S. Liu, J. Guo, Z. Li, and P. Lu, "Sensitivity-enhanced pressure sensor with hollow-core photonic crystal fiber," J. Lightwave Technol. **32**(23), 4035–4039 (2014).
17. Z. L. Ran, Y. J. Rao, W. J. Liu, X. Liao, and K. S. Chiang, "Laser-micromachined Fabry-Perot optical fiber tip sensor for high-resolution temperature independent measurement of refractive index," Opt. Express **16**(3), 2252–2263 (2008).
18. X. Zhang, H. Pan, H. Bai, M. Yan, J. Wang, C. Deng, and T. Wang, "Transition of Fabry–Perot and antiresonant mechanisms via a SMF-capillary-SMF structure," Opt. Lett. **43**(10), 2268–2271 (2018).
19. S. Liu, K. Yang, Y. Wang, J. Qu, C. Liao, J. He, Z. Li, G. Yin, B. Sun, J. Zhou, G. Wang, J. Tang, and J. Zhao, "High-sensitivity strain sensor based on in-fiber rectangular air bubble," Sci. Rep. **5**(1), 7624 (2015).
20. M. S. Ferreira, J. Bierlich, J. Kobelke, K. Schuster, J. L. Santos, and O. Frazão, "Towards the control of highly sensitive Fabry-Pérot strain sensor based on hollow-core ring photonic crystal fiber," Opt. Express **20**(20), 21946–21952 (2012).